Neural Network-Enabled Multiparametric Impedance Signal Templating for High throughput Single-Cell Deformability Cytometry Under Viscoelastic Extensional Flows

Javad Jarmoshti, Abdullah-Bin Siddique, Aditya Rane, Shaghayegh Mirhosseini, Sara J. Adair, Todd W. Bauer, Federica Caselli,* and Nathan S. Swami*

Cellular biophysical metrics exhibit systematic alterations during processes, such as metastasis and immune cell activation, which can be used to identify and separate live cell subpopulations for targeting drug screening. Image-based biophysical cytometry under extensional flows can accurately quantify cell deformability based on cell shape alterations but needs extensive image reconstruction, which limits its inline utilization to activate cell sorting. Impedance cytometry can measure these cell shape alterations based on electric field screening, while its frequency response offers functional information on cell viability and interior structure, which are difficult to discern by imaging. Furthermore, 1-D temporal impedance signal trains exhibit characteristic shapes that can be rapidly templated in near real-time to extract single-cell biophysical metrics to activate sorting. We present a multilayer perceptron neural network signal templating approach that utilizes raw impedance signals from cells under extensional flow, alongside its training with image metrics from corresponding cells to derive net electrical anisotropy metrics that quantify cell deformability over wide anisotropy ranges and with minimal errors from cell size distributions. Deformability and electrical physiology metrics are applied in conjunction on the same cell for multiparametric classification of live pancreatic cancer cells versus cancer associated fibroblasts using the support vector machine model.

1. Introduction

The phenotypic heterogeneity of cancer, immune and stem cell systems[1] that exhibit subpopulations to serve their multiple functions,[2] highlights the need for tools capable of quantifying and separating such subpopulations.[3] Cell surface markers enable phenotypic quantification by flow cytometry after binding to fluorescently labeled antibodies. However, markers are not available for many cell phenotypes, while the sample preparation steps are time consuming, require costly chemicals, introduce a degree of selection bias, and can adversely affect maintenance of cell viability within longitudinal studies.[4] Cellular biophysical properties,[5] such as their size distribution, deformability, membrane morphology, and nucleus to cell size are correlated in many contexts to cell function. Since they do not require labeling, they present a complementary set of metrics to identify and separate live cell subpopulations, with minimal sample preparation. Biomechanical properties of cancer cells are particularly of interest for identifying metastatic subpopulations,[6] since the early-stage in the metastasis of solid tumors is associated with stiffening of the tumor microenvironment (TME),[7] which is detected by cell mechano-sensing pathways[8] to cause systematic alterations in cellular deformability.[9] Hence, these metrics can potentially be used to identify and sort metastatic cells for targeting the screening of drugs that inhibit metastasis.[10] This is especially relevant in

J. Jarmoshti, A.-B. Siddique, S. Mirhosseini, N. S. Swami
Electrical & Computer Engineering
University of Virginia
Charlottesville, VA 22904, USA
E-mail: nswami@virginia.edu

A. Rane, N. S. Swami
Chemistry, University of Virginia
University of Virginia
Charlottesville, VA 22904, USA

S. J. Adair, T. W. Bauer
Surgery, School of Medicine
University of Virginia
Charlottesville, VA 22903, USA

F. Caselli
Civil Engineering and Computer Science
University of Rome Tor Vergata
Rome 00133, Italy
E-mail: caselli@ing.uniroma2.it

pancreatic cancer (from pancreatic ductal adenocarcinoma or PDAC) that is the third leading cause of cancer deaths,[11] due to its propensity for tumor metastasis.[12] Mechanical properties are essential to PDAC cell metastasis[13] due to its highly fibrotic and poorly vascularized TME.

Contactless single-cell deformability cytometry is often conducted under microfluidic viscoelastic flows that cause shear,[14] extensional[15] or compressive forces,[16] using high-speed imaging to measure alterations in cell anisotropy.[17–19] While high-speed imaging provides accurate spatial information on cells, it is not well-associated with their functional attributes, such as cell viability. Furthermore, due to the size, interior shape, and compositional diversity of cellular subpopulations, it is challenging to acquire focused single-cell images at high throughput for quantification of cell deformability. Hence, extensive image reconstruction is required,[20,21] which is often conducted offline, thereby limiting its utilization in near real-time to activate sorting.[22] Impedance cytometry for single-cell biophysical analysis,[23–25] has been associated with cell function within many contexts, such as immune cell activation,[26,27] red blood cell infection[28,29] cell health,[30] classification of apoptotic states of cancer cells[31,32] altered nucleus to cell size to monitor stem cell cycle characteristics,[33] and cancer cell subpopulations after co-culture with associated fibroblasts.[34] Prior work on deformability-based classification by impedance analysis has used constrictions to cause cell deformation[35,36] which is limited by the broad cell size distributions in typical samples and the associated clogging that limits throughput. Viscoelastic cross-flows address this limitation,[37] but the cell deformation is instantaneous and the dynamic range for anisotropy modulation is limited, which motivates this work on impedance cytometry under hyperbolic extensional flows for contactless and progressive single-cell deformation to high shape anisotropies (≈3-fold). Furthermore, unlike 2D image information that requires extensive signal processing, 1D temporal impedance signals exhibit characteristic shapes[38] that can be rapidly templated using neural networks to extract single-cell metrics[39,40] such as size, anisotropy, velocity, membrane capacitance and cytoplasmic conductivity for enabling high throughput biophysical measurement and selection.

In this work, using viscoelastic hyperbolic extensional flows[41–43] that cause high throughput (≈100 cells s^{-1} at 1–2×10^6 cells mL^{-1}), contactless and clog-free cell focusing, spacing and progressively greater cell deformation over the extensional flow length,[44] the shape anisotropy of pancreatic cancer cells and cancer associated fibroblasts (CAFs) are measured by impedance and image cytometry over their wide cell size distributions. While neural networks have been used on thresholded impedance signals to identify relationships between cellular biophysical metrics[45,46] our innovation is the utilization of a multilayer perceptron (MLP) neural network for processing raw impedance signals of diverse shapes after its training with image cytometry data from the same cell for accurate and rapid signal templating to quantify cell deformability. The interrelationship between impedance signal metrics for quantifying cell shape anisotropy under microfluidic deformation is first elucidated using simulations of electric field screening and then optimized using the MLP network to fit measured impedance data, alongside training of the network with image cytometry data from the same

cell to extract a net electrical anisotropy index (EAI) that quantifies cell deformability over a wide range of anisotropies (1-3-fold) and with minimal errors from their wide size distributions (10–25 µm), as validated against image metrics using cancer cells and CAFs. Since cellular electrical physiology from the impedance frequency response of its magnitude ($|Z|$) and phase (ϕZ) offers orthogonal metrics for cell phenotypic recognition based on apoptosis, membrane folding and interior structure, the EAI metric is applied in a multiparametric manner with cell electrical physiology using the support vector machine (SVM) model to distinguish live cancer cells versus CAFs derived from the same metastatic patient. This is significant for identifying drug resistant cancer cell subpopulations that arise due to interaction with CAFs under drug treatment.[47,48] Given the potential of neural networks for rapid impedance signal templating[39] and specificity of impedance spectra to cell phenotypes,[40] this work advances its coupling with image data for the accurate extraction of cellular biophysical metrics in a multiparametric manner to activate sorting for isolation of rare cell subpopulations from dilute samples with unknown phenotypes.[49]

2. Results

2.1. Dependence of Cell Anisotropy Measurement Under Deformation on Cell Size

Clinically relevant samples of cancer,[50] immune,[51] and stem cells[33] that exhibit phenotypic plasticity show wide cell size distributions (10–25 µm), which makes it challenging to measure cell biomechanical metrics in microchannels.[52] To illustrate the effect of cell size distributions on impedance metrics for measurement of deformation-induced cell anisotropy alterations over a wide range (1-3-fold), we use electric field simulations to obtain impedance signals. This is simulated based on sets of coplanar electrodes that are patterned at the floor of the pre-deformation, deformation and recovery zones of a microfluidic hyperbolic extensional flow to create progressively higher levels of deformation along its length (**Figure** 1A), with sufficient length available for single-cell correspondence to imaging cytometry. Since impedance signal trains show a typical bipolar signal shape under differential amplification, we focus on the metrics of signal amplitude and width in the respective zones (Figure 1B). It is noteworthy that the utilization of viscoelastic flows (2% polyethylene-oxide or PEO with 1x phosphate buffered saline or PBS) enables elasto-inertial particle focusing across the microchannel cross-sectional depth,[53] thereby minimizing positional dependence for measurement by coplanar electrodes. This is apparent from the widely dispersed multiple data clusters of impedance phase versus particle size in 1x PBS (Figure S1A, Supporting Information) that become narrow single data clusters corresponding to 12 µm and 15 µm particles (Figure S1B, Supporting Information). Using electric field screening simulations (Figure 1C) of model spherical particles with a unitary image-based anisotropy index or AI in the pre-deformation zone (i.e., $A_1 = B_1$), a relatively higher anisotropy index at the end of the deformation zone ($AI = A_2/B_2>1$) and returning to unity in the recovery zone, we plot the simulated impedance signal amplitude (M_1, M_2 in Figure 1Di) and signal width (2σ levels in Figure 1Dii) as a function of varying anisotropies (1-3-fold) and over wide cell size
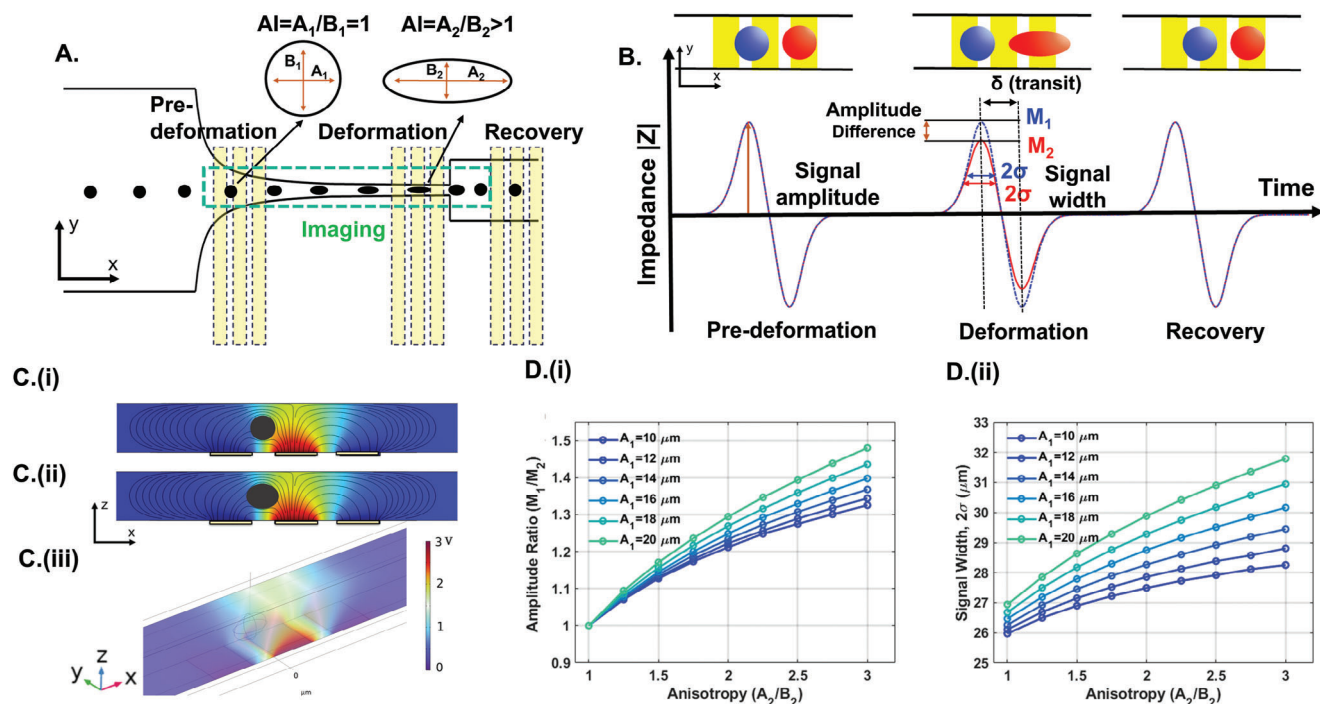
Figure 1. Overview of device simulations to compute impedance signal metrics. A) Progressive deformation of cells under viscoelastic hyperbolic extensional flow causes alterations to their anisotropy index (AI), as defined by ratio of its length (*A*) to width (*B*) in the flow direction, which is measured in the region prior to deformation (zone 1), during deformation (zone 2) and post-recovery (zone 3) using co-planar electrodes at channel floor, as well as by imaging (dashed box). B) Impedance signals of particles over the respective zones shows that the non-deformable particle (blue) exhibits invariant signals, while elongation of the deformable particle (red) along its length and width causes systematic alterations in impedance signal amplitude and width. C) Simulated electric potential distribution inside the channel (25×30 μm) with coplanar electrodes (25 μm width and 15 μm spacing) for: (i) non-deformable, and (ii) deformable particles,(iii) using 3D simulations. D) Impedance signal metrics for particles with anisotropies of 1 to 3 as a function of electrical size: (i) Signal amplitude, and (ii) Signal width.

distributions (10-20 μm). While the metrics of signal amplitude ratio and width increase as expected with particle anisotropy, their strong dependence on particle size is apparent, making it challenging to attribute the alterations in their metrics to anisotropy ratios versus to particle sizes. Hence, we subsequently utilize fitting methods on simulation data to identify functions of the respective impedance metrics that reduce the error from the wide cell size distributions and then optimize this approach using neural network-based signal templating on simulated and experimental data.

2.2. Electrical Anisotropy Metric for Deformation Under Wide Cell Size Distributions

We seek to develop a composite metric for transducing deformed cell shape anisotropy over a wide range (1-3-fold), with minimal errors from the wide cell size distributions observed in typical biological samples. For particle dimensions of *A, B,* and *C* along the channel length (x-axis), width (y-axis), and depth (z-axis) that start out as spherical within the pre-deformation zone (**Figure 2Ai**) and become ellipsoidal in the deformation zone (Figure 2Aii), we assume that its projected area in the xy plane (i.e., $\frac{\pi}{4}AB$) and its volume do not change during deformation (i.e., volume conservation). This is justified based on our image cytometry results (Figure S2, Supporting Information) that show a

linear plot of unity slope for the data clusters in the deformation zone (A_2B_2) versus in the pre-deformation zone (A_1B_1 in Figure S2A, Supporting Information) and versus in the recovery zone (A_3B_3 in Figure S2B, Supporting Information), with comparison in Figure S2E (Supporting Information). Plots of the ratio of A_1B_1 to A_2B_2 in Figure S2C (Supporting Information), and that of A_3B_3 to A_2B_2 in Figure S2D (Supporting Information) yield a linear data cluster of zero slope that is centered at unity. Hence, combining the volume conservation assumption (Equation (1)) with observations on the ratio of the product of *A* and *B* in the respective deformation zones (Equation (2)), we can infer that all particle deformations occur only along the channel length and width, with minimal alterations along the depth (Equation (3)). Recalling that $A_1 = B_1$, the anisotropy index (*AI* that depends on particle length to width ratios in the deformation zone) can be rewritten solely in terms of particle length, per Equation (4).

$$A_1.B_1.C_1 = A_2.B_2.C_2 = A_3.B_3.C_3 \tag{1}$$

$$\frac{A_1.B_1}{A_2.B_2} = 1; and \frac{A_3.B_3}{A_2.B_2} = 1 \tag{2}$$

$$\Rightarrow C_1 = C_2 = C_3 \tag{3}$$

$$AI = \frac{A_2}{B_2} \Rightarrow AI = \left(\frac{A_2}{A_1}\right)^2 \tag{4}$$
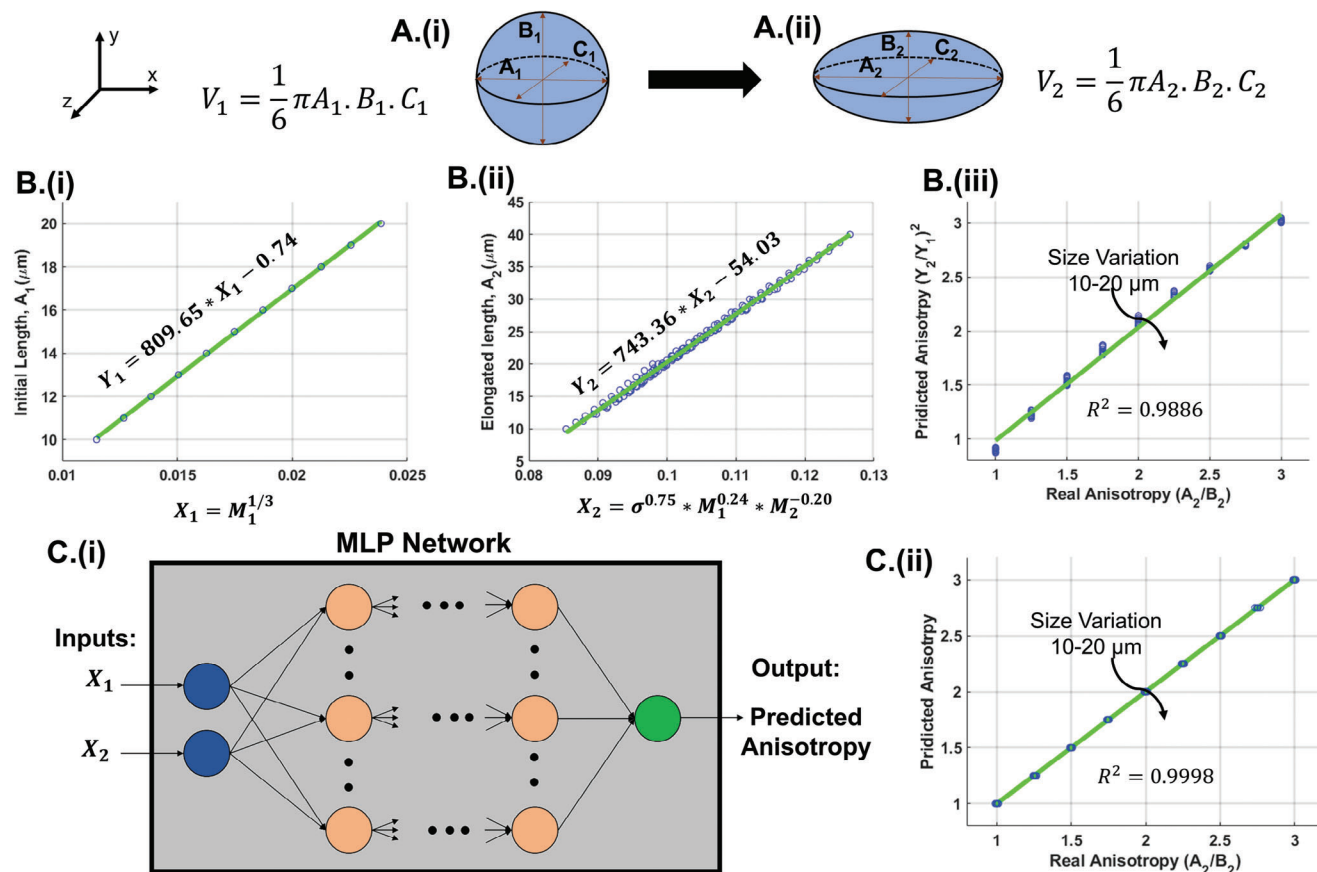
Figure 2. Using impedance signal magnitude and width to compute a composite metric to predict anisotropy: A) (i) initial and (ii) deformed particle dimensions, B) Fitting method applied to: (i) Pre-deformation zone to compute initial length of spherical particle,(ii) Deformation zone to compute elongated length of ellipsoidal particle,(iii) Comparing predicted versus real particle anisotropy over a range of particle sizes. C).(i) Multilayer perceptron (MLP) neural network with an input of signal amplitudes and widths and an output of predicted anisotropies that is optimized for fitting such functions (ii).

To compute a composite metric for the particle shape anisotropy under deformation, with minimal errors from particle size variations, we start with computing a fitting function between the elongated particle length (A_2), using exponentials of impedance signal amplitudes (M_1, M_2) and width (2σ) to fit impedance signal simulations (Figure 2B), and then generalize this approach using a multilayer perceptron (MLP) neural network that is optimized for fitting (Figure 2C). From prior work,[54] it is known that the initial particle length in the pre-deformation zone (A_1) exhibits a cube-root dependence on impedance magnitude (i.e., $M_1^{1/3}$), per Equation (5), to obtain a fitted linear plot in Figure 2Bi. Using the logarithmic regression method (see equation in caption of Figure S3, Supporting Information) to find the non-linear relationship between impedance signal parameters in the pre-deformation and deformation zones, a relationship between signal amplitudes (M_1 and M_2), width (2σ) and particle length (A_2) in the respective zones can be written per Equation (6) (see, Figures S3,S4, Supporting Information), which can also be computed as a fitted linear plot in Figure 2Bii to reduce errors from size variations (Figure 2Biii).

$$A_1 \sim Y_1 = m_1 X_1 + c_1; wherein : X_1 = M_1^{1/3} \quad (5)$$

$$A_2 \sim Y_2 = m_2 X_2 + c_2; wherein : X_2 = \left(\sigma^{0.75} * M_1^{0.24} * M_2^{-0.20} \right) \quad (6)$$

A more generalized approach can be followed by using a multilayer perceptron (MLP) neural network that is optimized for fitting such functions (Figure 2Ci; Figure S4A, Supporting Information). Using inputs of the X-axes from the plots in Figure 2Bi,ii, the output of predicted anisotropies is computed based on simulated (Figure S4B, Supporting Information) and experimental data (Figure S4C,D, Supporting Information). In fact, the utilization of signal amplitude and width metrics is essential for obtaining higher R^2 values (Figure S4D, Supporting Information) than using signal amplitude metrics only (Figure S4C, Supporting Information). In this manner, the composite metric determined using the MLP network can predict the anisotropy over a wide range (1-3-fold), with minimal dependence on cell sizes (Figure 2Cii). While the fitting method (Figure 2B) is limited when the relationship between $(Y_2/Y_1)^2$ and the cell shape anisotropy deviates from a linear model, the MLP network (Figure 2C) can learn the non-linear relationship between the inputs and output using multiple hidden layers, with a non-linear activation function, thereby achieving a higher R^2 value, due to its inherent complexity and flexibility.

ADVANCED
SCIENCE NEWS

www.advancedsciencenews.com
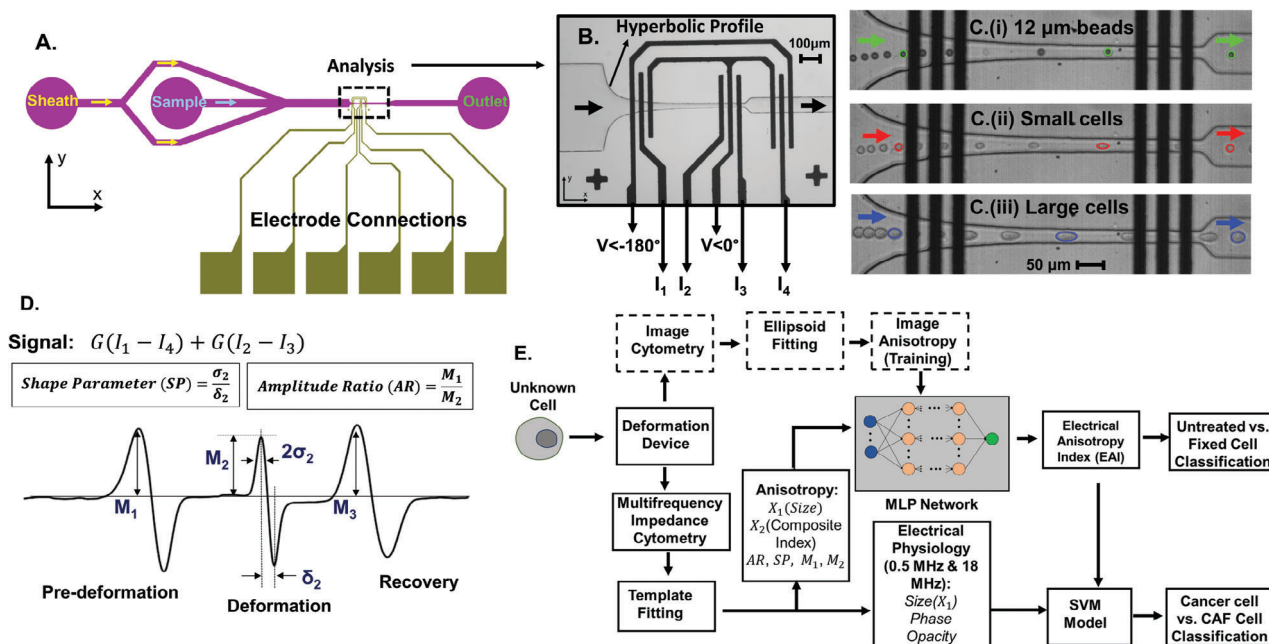
NANO · MICRO
small

www.small-journal.com

Figure 3. Device operation and signal analysis. A) Fluidics for sample and sheath flows showing the impedance and image analysis region. B) Analysis region with hyperbolic extensional flow and the electrical wiring for signal acquisition. C) Time-lapse high-speed images of deformation of: (i) 12 µm beads (green),(ii) small cells (≈12 µm –red), and (iii) large cells (≈20 µm – blue). D) Impedance signal trains indicating the respective amplitudes (M), widths (2σ) and transit times (δ) of the particle in the pre-deformation, deformation, and recovery zones to measure anisotropy based on input metrics of amplitude (M_1, M_2, M_3) and shape parameter (σ_2/δ_2). E) A Multilayer perceptron (MLP) neural network trained with impedance and image cytometry data is used to derive a net electrical anisotropy index (EAI) for signal templating to extract cell shape anisotropy in the deformation zone. The EAI can be combined with electrical physiology metrics of the corresponding cells to classify live cancer cells versus CAFs, using the SVM model.

2.3. Electrical Anisotropy Index of Deformability by Coupling with Image Metrics

Using the MLP neural network, the impedance-based anisotropy determined from the input of composite metrics (X_1 from Figure 2Bi and X_2 from Figure 2Bi) is coupled with the image anisotropy index (*AI* of Figure 1A computed by fitting an ellipse to calculate *A* and *B* in each zone) from cytometry data with single-cell correspondence between the respective metrics, to derive a net electrical anisotropy index (EAI) for deformability. This is implemented using a microfluidic chip (**Figure 3A,B**) with sheath and sample flows that lead to a hyperbolic profile for measurement of cell shape anisotropy under viscoelastic extensional flow using single-cell impedance and image cytometry of corresponding cells. The analysis region under hyperbolic extensional flow (Figure 3B) shows the voltage application and current measurement points in the pre-deformation, deformation, and recovery zones. Image acquisition occurs over the pre-deformation to the recovery zones (per dashed box in Figure 1A), with cross-correlation of image and impedance signal trains used for data synchronization (Figure S5A, Supporting Information). Typical image cytometry results (Figure 3C) are indicated as time-lapse measurements of non-deformable 12 µm polystyrene beads (green), equivalently sized small cancer cells (red) and larger sized (≈20 µm) cancer cells (blue) in the respective zones. The impedance signal measured at 0.5 MHz from currents: I_1, I_2, I_3 and I_4, is shown in Figure 3D for particles in the pre-deformation, deformation, and recovery zones, alongside their respective signal metrics of amplitudes (M_1, M_2, M_3), signal

widths ($2\sigma_1$, $2\sigma_2$, $2\sigma_3$) and transit times (δ_1, δ_2, δ_3). Since the cell electrical size is proportional to image size over the cell size distribution in the sample (Figure S6A, Supporting Information) and the cell velocity determined from impedance signals decreases with cell size (Figure S6B (Supporting Information), per velocity profile simulations in Figure S6E,F, Supporting Information), the impedance signal trains can be aligned by velocity normalization to convert them from time domain (Figure S5B, Supporting Information) to position domain, along the length or X-axis (Figure S5C, Supporting Information). In this manner, signal templating can extract the respective signal metrics based on the amplitude ratios ($AR = M_1/M_2$) and shape parameters ($SP = \sigma_2/\delta_2$) for neural network-based implementation after training with image metrics (including back to spherical shape in recovery zone), for computing the EAI to measure cell shape anisotropy (Figure 3E) for deformability-based distinction (e.g., untreated vs fixed cells). For image-based classification using the SVM model (e.g., cancer cells vs CAFs), the metrics of single-cell size and anisotropy (*A* and *B* per Figure 1A) were used. However, due to presence of some dead cells in typical cancer cell samples that broaden the deformability distributions (discussed later in Figure 6; Figure S9, Supporting Information), only live cells were gated in, using ϕZ metrics. For impedance-based classification, the neural network derived EAI was used for deformability and combined with electrical physiology from the impedance frequency response (size or $\sqrt[3]{|Z|_{0.5\,MHz}}, \phi Z_{0.5\,MHz}$ & $\phi Z_{18\,MHz}$, and magnitude opacity or $|Z|_{18\,MHz}/|Z|_{0.5\,MHz}$) for distinction based on cell viability and interior structure.
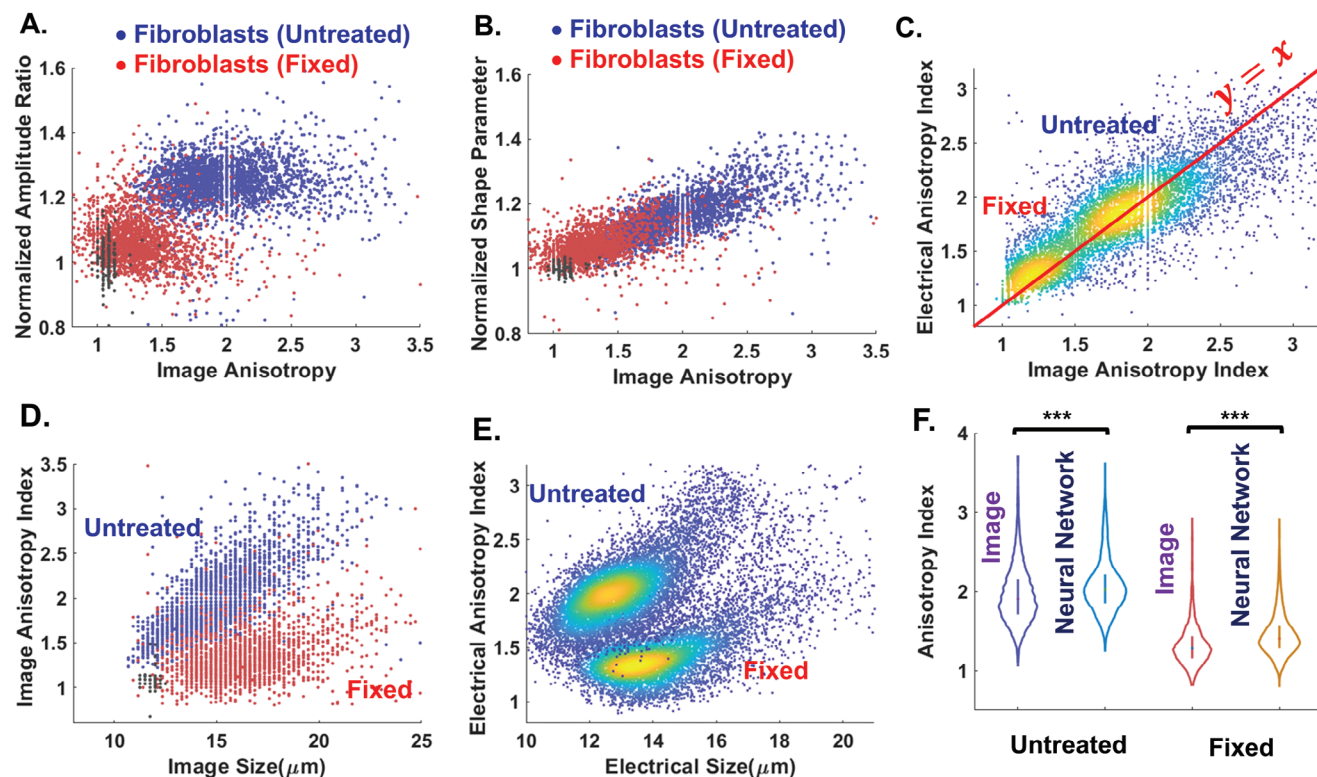
Figure 4. Validation of impedance versus image metrics for cell shape anisotropy under hyperbolic extensional flow using untreated and fixed cancer associated fibroblasts (CAFs), with beads as black symbols. A) Plateauing of impedance amplitude ratio at high image anisotropies, B) Linear rise in impedance shape parameter with image anisotropy over measured range, C) The neural network derived impedance signal templating to extract electrical anisotropy index (EAI) after training with image cytometry data shows near-equivalent cell anisotropy levels based on comparison of shape anisotropy from image cytometry D) to EAI from impedance cytometry E), with comparison of their significance F): *** p < 0.001 (≈2000 events per sample type for image data and ≈8000 events per sample type for impedance data).

2.4. Validation of Deformed Electrical Anisotropy Index Versus Image Metrics

The net electrical anisotropy index (EAI) under hyperbolic extensional flow deformation obtained from the neural network is validated against image-based anisotropy metrics using cancer associated fibroblasts (CAFs) obtained from a metastatic patient-derived tumor (T608),[55] measured in untreated and fixed states. It is apparent from **Figure 4A** that the metric of impedance signal amplitude ratio distinguishes untreated versus fixed fibroblasts, but the signal plateaus off at higher image anisotropy levels, whereas the impedance signal shape metric rises linearly with image anisotropy over the entire measured range (Figure 4B). The neural network-based electrical anisotropy index (EAI) after training with image metrics is able to obtain near-equivalent cell anisotropy levels, as apparent from the unity slope of the comparison plot in Figure 4C ($R^2 = 0.9$). Per the image cytometry results (Figure 4D), fibroblasts shows a broad size range (≈11–18 μm) and exhibit a broad range of cell shape anisotropies under hyperbolic extensional flow deformation (1-3-fold) in the untreated state, while fixed cells show only a mild increase in cell shape anisotropy. The cell shape anisotropy measured from the respective impedance signals after neural network templating to extract the composite metric shows a

similar trend (Figure 4E), as summarized in the violin plot of Figure 4F. Impedance metrics are also able to measure cell anisotropy alterations from deformation to the recovery zones (Figure S7B, Supporting Information), based on similarity of their trends to image cytometry (Figure S7A, Supporting Information).

To illustrate merits of the respective deformability metrics based on the impedance amplitude ratio (M_1/M_2), shape parameter (σ_2/δ_2) and the neural network-derived EAI, we compare data from CAFs (**Figure 5A**) to cancer cells that exhibit even broader size distributions (12–21 μm in Figure 5B). While the amplitude ratio metric does not exhibit the expected steady increase with cell size for fibroblasts (Figure 5Ai) and cancer cells (Figure 5Bi), as expected from simulations Figure 1Di, this trend is apparent for the shape parameter (Figure 5Aii) and the EAI metrics (Figure 5Aiii, as expected from the simulations (Figure 1Dii), thereby improving distinction of the untreated versus fixed cell populations for fibroblasts (Figure 5Aii) and cancer cells (Figure 5Bii). The respective cell populations exhibit a further improvement in distinction based on the neural network-derived EAI that shows a wider range of anisotropies, resembling the data from image metrics for fibroblasts (Figure 5Aiii) and cancer cells (Figure 5Biii).

ADVANCED
SCIENCE NEWS

www.advancedsciencenews.com
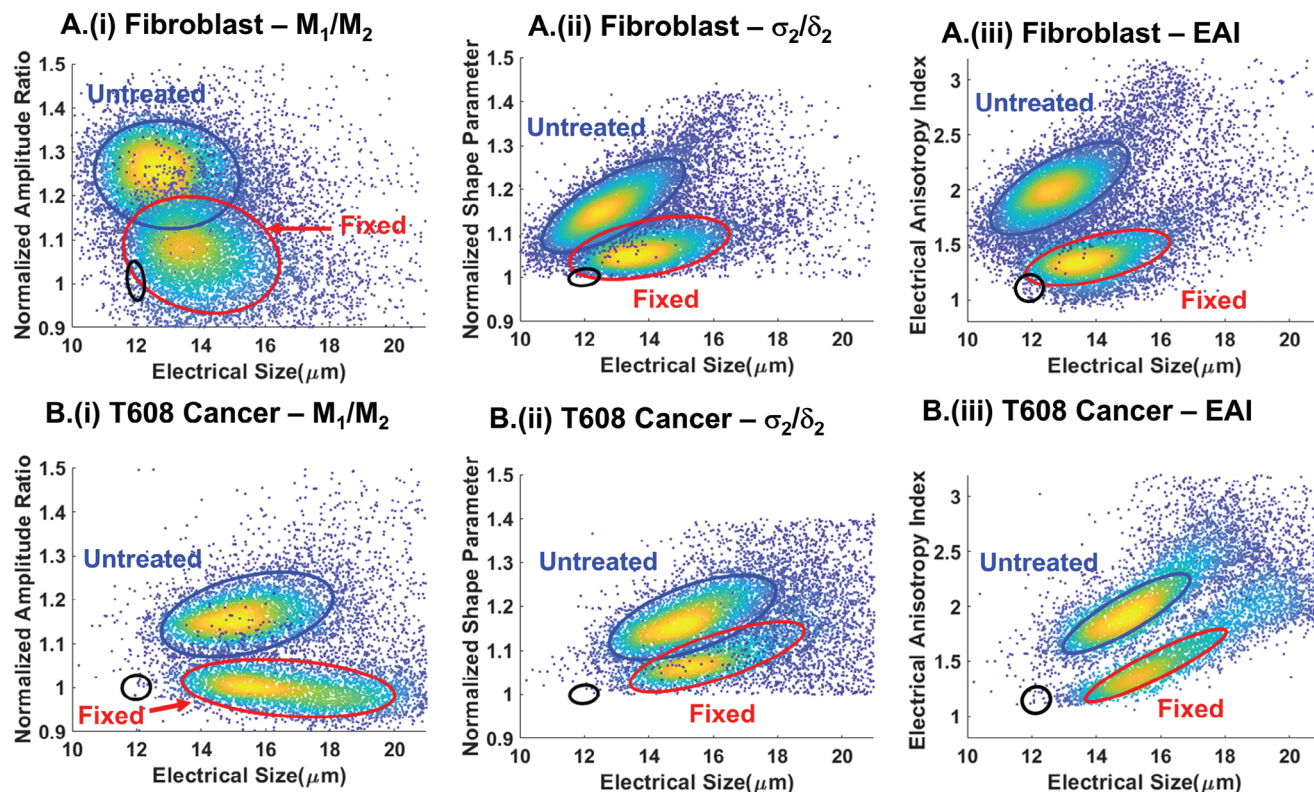
NANO · MICRO
small

www.small-journal.com

Figure 5. Impedance metrics for measurement of deformed cell shape anisotropy based on impedance signal amplitude ratio (M_1/M_2) in column (i), shape parameter (σ/δ) in column (ii), and the neural network-derived electrical anisotropy index (EAI) in column (iii) for A) Cancer associated fibroblasts (CAFs), and B) Cancer cells. The ellipses around the respective data clusters illustrate the Gaussian distribution for polystyrene beads (black – 50% density plots), untreated (blue – 90% density plots), and fixed cells (red – 90% density plots), with ≈7000–8000 events per sample type.

2.5. Combining Deformability and Electrical Physiology Metrics for Cell Distinction

Electrical physiology from the impedance frequency response (electrical size or $\sqrt[3]{|Z|_{0.5\,MHz}}$, impedance phase or $\phi Z_{0.5\,MHz}$ & $\phi Z_{18\,MHz}$, and magnitude opacity or $|Z|_{18\,MHz}/|Z|_{0.5\,MHz}$) can provide an orthogonal set of metrics for identifying cellular phenotype that is often not reflected within their deformability properties (e.g., EAI metric), thereby motivating our consideration of combination of these metrics for cell recognition using impedance cytometry. A prime example is cell viability, which is significant to detect for quantifying drug resistant subpopulations, since cultures of patient-derived cancer cells that are enlarged within xenograft models often exhibit a background of apoptotic cells in their untreated state, which further increases under drug-treatment. Our prior work with pancreatic cancer cells has shown that the ratio of the impedance phase at low ($\phi Z_{0.5\,MHz}$) to high frequency ($\phi Z_{18\,MHz}$) can be used to quantify apoptotic cells,[31] as validated by flow cytometry after staining for Annexin V, since these metrics are highly sensitive to alterations in dielectric polarization of the plasma membrane of apoptotic cells.[56] Using this metric, we can infer that cell viability is not altered under viscoelastic extensional flows, since the number of non-viable cancer cells is unchanged between the pre-deformation, deformation and recovery regions (Figure S8, Supporting Information). It is apparent that

cancer cells in the untreated state include some apoptotic cells (**Figure 6Ai**), which substantially increase in their drug-treated state (Figure 6Bi) due to apoptotic cells released from their adherent culture (Figure 6Ci). Apoptotic cells, in general, show lower deformability (Figure 6Aii,Bii,Cii), but their wide size distribution broadens their cell deformability distribution, as apparent in Figure S9 (Supporting Information). Hence, impedance phase metrics ($\phi Z_{0.5\,MHz}$ & $\phi Z_{18\,MHz}$ per Figure 6Ai,Bi,Ci) were used to gate in live cell events only, and exclude apoptotic events for SVM classification of cancer cells versus CAFs based on image and impedance based metrics. For live cells, these impedance metrics also contain information on interior structure for distinction of pancreatic cancer cells versus CAFs. At lower frequencies (0.5 MHz) wherein cell membrane induced field screening dominates the impedance response, CAFs exhibit lower electrical size and lower ϕZ in comparison to cancer cells (Figure S10, Supporting Information), while CAFs exhibit higher magnitude opacity and ϕZ levels at higher frequencies (18 MHz) due to passage of electric fields to the cell interior. Using only live cells events, the image metric (**Figure 7A**) and the EAI metric (Figure 7B) can distinguish the higher deformability of CAFs versus cancer cells. The SVM model classification results (Figure 7C) with positive predictive values or PPV and negative predictive values or NPV in Figure S11 (Supporting Information) show that the neural network-derived EAI metric performs better than the component impedance amplitude ratio and shape parameter metrics, and is
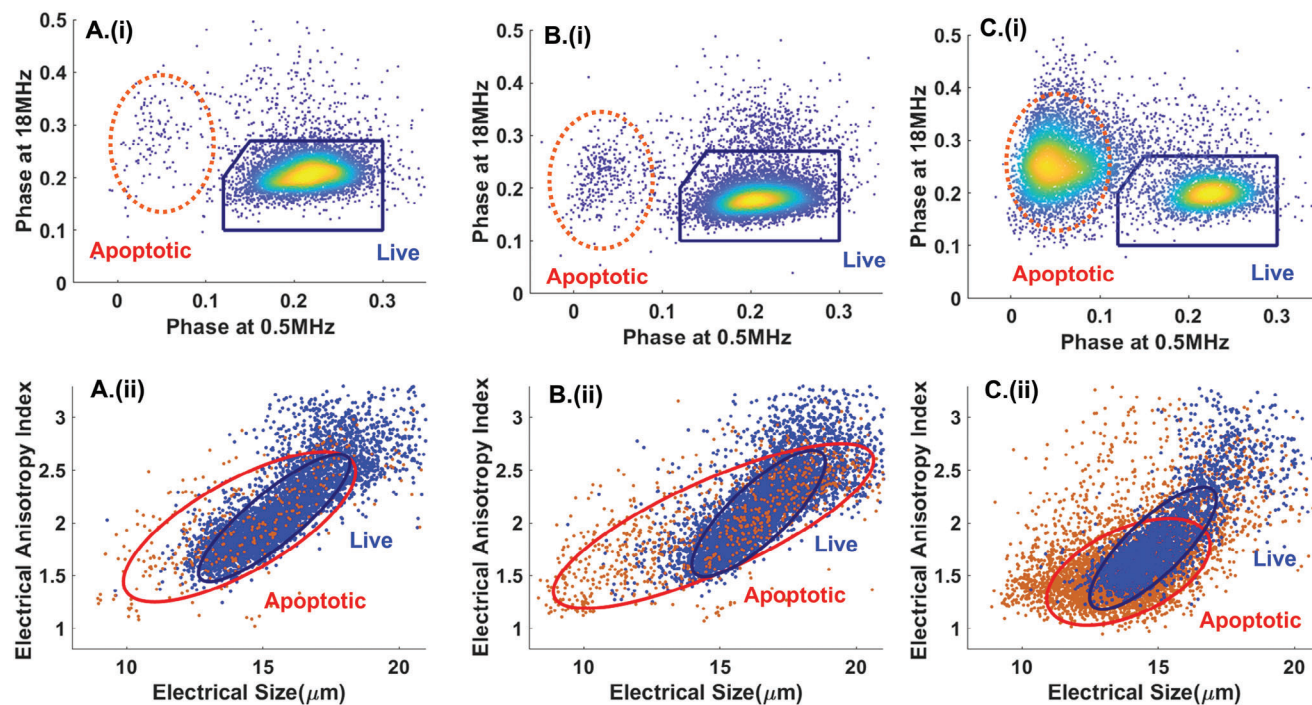
ADVANCED
SCIENCE NEWS
www.advancedsciencenews.com

NANO · MICRO
small
www.small-journal.com

Figure 6. Impedance phase (ϕZ) at 18 MHz versus 0.5 MHz is used to classify live versus apoptotic cells based on: A) (i) untreated, and B) (i) gemcitabine-treated (1µg mL^{-1}) cultures that include the apoptotic cells released from the adherent culture in C) (i). Cell deformability measured through the EAI metric exhibits broader distributions upon inclusion of apoptotic cells with live cells, as apparent after gating the live versus apoptotic events (Figure Aii, Bii, Cii) using their respective ϕZ data (Figure Ai,Bi,Ci), with ≈7000 events per sample type and the gate outlines for each sample type enclosing >90% of the data.

comparable to the combined image metrics obtained after gating in live cells. The combined electrical metrics from the EAI and electrical physiology perform better than the EAI only, and the classification is on par with the combined image metrics used to train the neural network.

3. Conclusion

Impedance signal templating strategies advance the vision of rapid inline extraction of cellular biophysical metrics from single-cell signal trains to quantify cell deformability and electrical physiology, as well as utilize this information to activate sorting. However, the wide cell size distributions within typical samples make it challenging to attribute the alterations in impedance metrics to deformed cell anisotropies versus to cell size variations. Hence, based on simulated data obtained from electric field screening in the microfluidic device, a fitting method and a neural network model are used to learn the non-linear relationships between the single-cell deformed particle width and length with the impedance signal amplitudes and widths in the pre-deformed, deformed and recovery regions for measuring cell deformation under viscoelastic extensional flow. In this manner, a composite impedance metric can be derived for measuring deformed cell shape over a wide range of anisotropies (1-3-fold) and with minimal errors from their wide cell size distribution (10–25 µm). This composite metric is then implemented with impedance signal trains from experimental data of cells deformed under viscoelastic hyperbolic extensional flows and trained with image

anisotropy data on corresponding cells using a multilayer perceptron neural network to enable computation of a net electrical anisotropy index or EAI that exhibits equivalent sensitivities to image cytometry data, after gating in live cell events only, as validated with pancreatic cancer cells and cancer associated fibroblasts. We chose the MLP network for training with image data to improve the accuracy for cell shape anisotropy quantification by impedance signal templating, since this network reduces computational time and enables near-sensor signal analysis for near real-time extraction of cell metrics to activate downstream sorting. In fact, coupling of the impedance signal amplitudes, widths, and transit times of cells in pre-deformation, deformation and recovery regions of the extension flow, as obtained by the net electrical anisotropy index, offers improved distinction ability between cell phenotypes of wide size distributions (10–25 µm), with cell shape recovery after deformation possibly offering information on the cytoskeleton viscosity.[57] However, electrical physiology based on impedance frequency response ($|Z|$, ϕZ at 0.5 and 18 MHz) can offer orthogonal metrics for identification of cell phenotype. For instance, the inclusion of apoptotic with live cancer cell events broadens their deformability distributions to limit their distinction, leading us to gate in live cell events for improving phenotypic distinction. Hence, while the EAI metric can distinguish the higher deformability of CAFs versus cancer cells, its application in conjunction with electrical physiology information from impedance frequency response on the same cell improves SVM-based classification, with performance parameters for the combined electrical metrics (Figure S11, Supporting
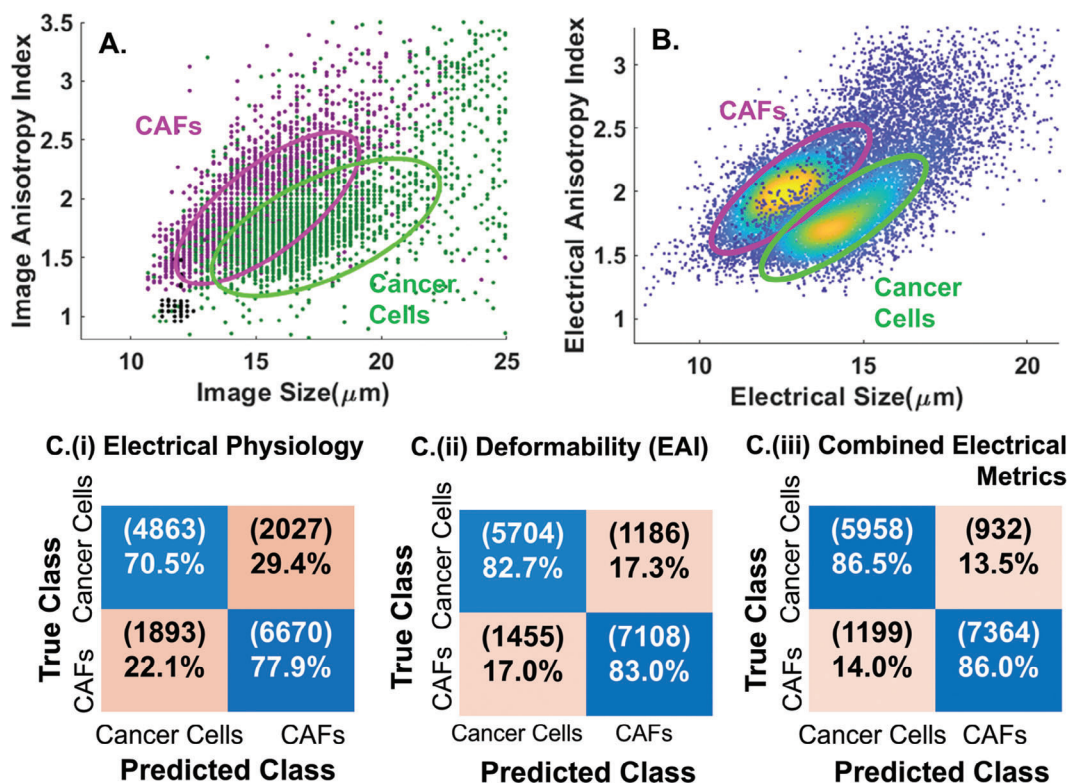
2407212 (8 of 12)

ADVANCED
SCIENCE NEWS
www.advancedsciencenews.com

NANO · MICRO
small
www.small-journal.com

Figure 7. Distinction of pancreatic cancer cells versus cancer associated fibroblasts (CAFs) derived from the same metastatic patient using: A) image-based deformability metrics (≈2000 events per sample type), B) neural network-derived electrical anisotropy index (EAI) (≈7000–8000 events per sample type), C) SVM classifier based on: (i) electrical physiology (electrical size or $\sqrt[3]{|Z|_{0.5\,MHz}}$, impedance phase or $\phi Z_{0.5\,MHz}$ & $\phi Z_{18\,MHz}$, and magnitude opacity or $|Z|_{18\,MHz}/|Z|_{0.5\,MHz}$), (ii) EAI from deformability, (iii) Combined electrical metrics from (i) and (ii). The confusion matrix for all metrics (impedance and image) shows the event numbers in brackets and the % values, with the respective sensitivity, positive predictive value (PPV), negative predictive value (NPV) and accuracy reported for each metric in Figure S11 and Table S1 (Supporting Information). To quantify efficiency of this classification, the ROC (receiver operating characteristic) curve and the AUC (area under curve) are presented in Figure S12 (Supporting Information).

Information) that are on par with the combined image metrics after gating in live cell events. The SVM model,[58] which can be extended for multi-class classification by using approaches such as "one-versus-one" or "one-versus-all", was chosen since it works well with smaller datasets to find the optimal separating hyperplane between classes, rather than classification methods that are better suited to larger datasets, which require more intensive computation. Given the potential of neural networks for rapid impedance signal templating and the specificity of the impedance frequency response to cell viability and interior structure, we envision that the reported image-based training method can improve taccuracy of cell deformability quantification and combined with multiparametric electrical physiology information for near real-time extraction of biophysical metrics to activate sorting of rare cell subpopulations with unknown phenotypes.

4. Experimental Section

Impedance Signal Simulations: The electric fields and currents were simulated by using COMSOL electric current module, using a rectangular channel design of 25 μm by 30 μm cross section, and three coplanar electrodes of 25 μm in width and 15 μm in spacing. A voltage signal of 3V_{pp} at 0.5MHz was applied to the middle electrode, while the voltage of the adjoining electrodes was maintained at ground level (0 V) for simulating the differential current. To simulate a deformable particle, a sphere

was passed across the electrodes in the pre-deformed region, followed by the same measurement in the deformed region as an ellipse of same volume and diameter in the z-axis, but differing anisotropy in image plane (xy-plane). The generated signal was fitted to a bipolar Gaussian function to determine its peak amplitude and signal width in MATLAB (R2022a, MathWorks). Separately, the shear rate and velocity within the hyperbolic channel was modeled in COMSOL laminar flow module.

Device Design and Integration: The microfluidic device with a hyperbolic extensional flow profile (Figure 3A,B) that constricts to 25 μm (> cell size) was fabricated by standard SU8 lithography (EVG 620) for PDMS micromolding and then aligned to gold electrodes that were patterned on a glass coverslip for bonding under an O_2 plasma (Tergeo Cleaner, PIE Scientific). A 3D printed holder was used to establish electrical contacts using a pogo pin assembly, with an open area to enable high speed imaging for image cytometry.

PDAC Cell Sample Preparation: PDAC tumor and CAFs samples from the anonymized patient, labeled MAD 08–608, were generated from remnant human tumor surgical pathology specimens in collaboration with the University of Virginia Biorepository and Tissue Research Facility. The protocol was approved through the University of Virginia Institutional Review Board (IRB) for Health Sciences Research (approval IRB-HSR number 13 529), and as part of the protocol, informed written consent of each participant was obtained for utilization of the tissue samples in this research. The tumor was propagated orthotopically in the pancreata of immuno-compromised mice, which was conducted in strict accordance with the Guide for the Care and Use of Laboratory Animals of the United States National Institutes of Health, per protocol 4078, approved by the Animal Care

**ADVANCED
SCIENCE NEWS**

www.advancedsciencenews.com

NANO · MICRO
small

www.small-journal.com

and Use Committee of the University of Virginia. The cells were transduced with firefly luciferase lentivirus (KeraFAST), selected using puromycin and maintained in RPMI 1640 with 10% FBS and 2 mM glutamine (complete medium), with fresh aliquots used for the reported experiments. For cell culture, cancer cells and CAFs were plated at an initial density of ≈500000 cells per 6 well plate and maintained in a media containing Dulbecco's Modified Eagle Medium (DMEM, Thermo Fisher Scientific), 10% Fetal Bovine Serum (Thermo Fisher), and 1% penicillin streptomycin (Thermo Fisher). The respective samples of fixed cells were prepared by suspending cells in 4% methanol-free formaldehyde for 8 min, followed by addition of 0.127 M glycine for 5 min to terminate the fixation.

PDAC Cell Drug Treatment: PDAC T608 cancer cells in monoculture were exposed to 1 µg mL^{-1} of gemcitabine (University of Virginia clinical pharmacy) for 48 h in complete medium. This drug condition was known to drive the cells under monoculture towards apoptosis.[31] Untreated control samples were kept under the same culture conditions and period as treated samples, for comparative analysis. Cells were trypsinized and analyzed by flow cytometry after fluorescent staining, and by impedance cytometry. Cell culture media was aspirated and stored to recover floating cells. The remaining adherent cells were washed in 1× PBS (Thermo Fisher) and enzymatically detached from the plate using 0.05% trypsin in 1× PBS for 10 min at 37 °C. The cells fractions were resuspended into a total volume of 5 mL DMEM with 10% FBS and 1% pen-strep (Thermo Fisher) and centrifuged at 300 g for 10 min. DMEM was then aspirated, and the cell pellet was resuspended in 1xPBS, 500 mM EDTA (Fisher Scientific), and 0.5% Bovine Serum Albumin (Sigma Aldrich) and filtered through a 100 µm cell strainer.

Measurement Set-Up for Impedance and Image Cytometry: To measure cell deformation in the microfluidic device under hyperbolic extensional flow, cells (concentration of ≈1−2 × 10^6 /mL) with co-flowing polystyrene beads (12 µm at a concentration of ≈1.2 × 10^5 /mL) were suspended in 2% (w/w) PEO solution and introduced via a syringe pump (neMESYS, Cetoni) into the sample inlet at a flow rate of 6 µL min^{-1}, accompanied by a sheath flow of 2% (w/w) PEO solution at the same flow rate from the sheath inlet, per Figure 3A. Single-cell impedance signals were measured at the pre-deformation, deformation, and recovery zones of the microfluidic channel using an impedance spectroscope (HF2IS, Zurich Instruments). In the deformation zone, the conventional differential measurement method was conducted by applying a voltage signal (at 0.5MHz and 18MHz, each with a magnitude of 3V$_{pp}$) to the middle electrode and measuring the differential current from the side electrodes via a differential current amplifier (HF2TA, Zurich Instruments). Electrode wiring in the pre-deformation and recovery zones was adjusted to enable impedance measurement using fewer channels by using two voltage signals of equal magnitude and frequency, but with opposite phases (0 and 180°) that were applied to the side electrodes, with currents at the middle electrodes measured using the same differential current amplifier. The signals were recorded for subsequent processing.

Signal Processing: The recorded impedance data were processed and analyzed utilizing MATLAB (R2022a, MathWorks). Initially, raw signals underwent filtering with a high pass filter to eliminate baseline and power line noise, along with a low pass filter for signal smoothing. Subsequently, a peak detection algorithm was implemented to identify events associated with cell passage through the electrodes. Each corresponding signal was then fitted to a bipolar Gaussian function to extract peak and signal width values across each zone (pre-deformation, deformation and recovery). Peak values were normalized against the mean peak value of 12 µm polystyrene beads, while signal width was normalized against particle transit time to determine the shape parameter that accounts for particle velocity. Following this, the shape parameter values were divided by the mean shape parameter of the 12 µm polystyrene beads. The amplitude and shape parameter values of the beads were scaled to unity. Typically, 6000–7200 events were detected over a 1-minute period in samples with 1–2×10^6 cells mL^{-1}, giving a measurement throughput of ≈100–120 particles s^{-1}. Of these 6000–7200 events, ≈5% were discarded during signal processing because they were not well fitted by a bi-polar Gaussian (R-square < 0.95), suggesting the occurrence of coincidences. The occurrence of coincidences depends on the expected number of particles in the sensing zone[44] ($\mu = cv$, wherein **c** was the sample concentration and **v** was the sensing zone volume). Plots of coincidences as a function of the cell concentration were computed in Figure S13A (Supporting Information) and measured in Figure S13B (Supporting Information), with the hyperbolic extensional flow spacing out coinciding events (Figure S13C, Supporting Information), which can be processed to improve their resolution.[44]

Image processing: A Phantom S210 camera connected to the Eurosys frame grabber card was utilized to capture video images in bright field mode. The recording utilized a resolution of 1280 by 256 pixels, a frame rate of 4000 fps, and an exposure time of 10 µs. Subsequently, custom Python code was utilized to process the frames, involving the subtraction of each frame from the reference frame, followed by the application of a weighted average kernel filter to enhance image quality. An event detection algorithm was then applied to identify particles passing through the channel, alongside an edge detection algorithm to measure anisotropy, achieved by fitting ellipses around the particles. Synchronization of image events with the impedance signal trains was accomplished using the cross-correlation method to align impedance and image events.

Neural Network and Machine Learning Implementation: A Multilayer Perceptron (MLP) neural network, configured with 30 hidden layers was implemented in MATLAB to train the network using the impedance metrics of electrical size, amplitude values, and the composite index that includes signal widths. Supervised learning was utilized with image anisotropy data to predict the electrical anisotropy index. Initially, 70% of the dataset, comprising 7930 events corresponding untreated and fixed fibroblast and cancer cells, was allocated for training, while the remaining 30% was reserved for testing the network's performance. Subsequently, another data set containing impedance metrics was utilized to evaluate the network's performance. Following the MLP neural network training, a Support Vector Machine (SVM) was employed to classify fibroblast and cancer cells according to their impedance metrics and deformability indexes. The SVM classification model underwent training utilizing 70% of a dataset, randomly selected from approximately 8000 fibroblast cells and 7000 cancer cells, with the remaining portion reserved for testing model accuracy. Prediction accuracy was evaluated by comparing the percentage of true classes against the predicted classes in total events.

Statistical Analysis: All data were presented as mean ± standard deviation (SD). Outliers were removed by considering data points that were farther than ±3 SD from the mean. To compare differences between two groups, a two-sample t-test was performed using MATLAB. The test was two-sided, with an alpha value set at 0.05. P-values less than this threshold were considered statistically significant, with significance levels reported as *p ≤ 0.05, **p ≤ 0.01, ***p ≤ 0.001. Error bars between cell types indicate the standard deviation between sample triplicates, with shape anisotropy correlation of impedance to image cytometry computed based on R^2 values.

Supporting Information

Supporting Information is available from the Wiley Online Library or from the author.

Conflict of Interest

The authors declare no conflict of interest.

Author Contributions

J.J. performed conceptualization, methodology, investigation, formal analysis, data curation, A.B.-S., A.R., S.M., and S.A. performed investigation, T.B. performed resources, supervision, F.C. performed methodology, formal analysis, wrote the original draft, supervision, N.S. performed conceptualization, methodology, formal analysis, resources, wrote the original draft, supervision, project administration, funding acquisition.

Data Availability Statement

The data that support the findings of this study are available in the supplementary material of this article.

Keywords

[1] T. J. Perkins, P. S. Swain, *Mol. Syst. Biol.* **2009**, *5*, 326.
[2] R. Satija, A. K. Shalek, *Trend. Immunol.* **2014**, *35*, 219.
[3] K. Klepárník, F. Foret, *Anal. Chim. Acta* **2013**, *800*, 12.
[4] J. Kling, *Nat. Biotechnol.* **2012**, *30*, 578.
[5] K. C. Lee, J. Guck, K. Goda, K. K. Tsia, *Trend. Biotechnol.* **2021**, *39*, 1249.
[6] G. Runel, N. Lopez-Ramirez, J. Chlasta, I. Masse, *Cells* **2021**, *10*, 887.
[7] A. C. Shieh, *Annal. Biomed. Eng.* **2011**, *39*, 1379.
[8] M. Maurer, J. Lammerding, *Ann. Rev. Biomed. Eng.* **2019**, *21*, 443.
[9] J. Kim, S. Han, A. Lei, M. Miyano, J. Bloom, V. Srivastava, M. R. Stampfer, Z. J. Gartner, M. A. LaBarge, L. L. Sohn, *Microsyst. Nanoeng.* **2018**, *4*, 1.
[10] A. A. Friedman, A. Letai, D. E. Fisher, K. T. Flaherty, *Nat. Rev. Cancer* **2015**, *15*, 747.
[11] L. Rahib, B. D. Smith, R. Aizenberg, A. B. Rosenzweig, J. M. Fleshman, L. M. Matrisian, *Cancer Res.* **2014**, *74*, 2913.
[12] A. Jemal, R. Siegel, E. Ward, Y. Hao, J. Xu, M. J. Thun, *Cancer J. Clin.* **2009**, *59*, 225.
[13] A. Chronopoulos, T. J. Lieberthal, A. E. del Río Hernández, *Conver. Sci. Phys. Oncol.* **2017**, *3*, 013001.
[14] O. Otto, P. Rosendahl, A. Mietke, S. Golfier, C. Herold, D. Klaue, S. Girardo, S. Pagliara, A. Ekpenyong, A. Jacobi, *Nat. Methods* **2015**, *12*, 199.
[15] F. J. Armistead, J. G. De Pablo, H. Gadêlha, S. A. Peyman, S. D. Evans, *Biophys. J.* **2019**, *116*, 1127.
[16] D. Dannhauser, M. I. Maremonti, V. Panzetta, D. Rossi, P. A. Netti, F. Causa, *Lab Chip* **2020**, *20*, 4611.
[17] P.-H. Wu, D. R.-B. Aroush, A. Asnacios, W.-C. Chen, M. E. Dokukin, B. L. Doss, P. Durand-Smet, A. Ekpenyong, J. Guck, N. V. Guz, *Nat. Methods* **2018**, *15*, 491.
[18] Y. Hao, S. Cheng, Y. Tanaka, Y. Hosokawa, Y. Yalikun, M. Li, *Biotechnol. Adv.* **2020**, *45*, 107648.
[19] M. Urbanska, H. E. Muñoz, J. Shaw Bagnall, O. Otto, S. R. Manalis, D. Di Carlo, J. Guck, *Nat. Methods* **2020**, *17*, 587.
[20] Y. Han, Y. Gu, A. C. Zhang, Y.-H. Lo, *Lab Chip* **2016**, *16*, 4639.
[21] H. Hua, S. Zou, Z. Ma, W. Guo, C. Y. Fong, B. L. Khoo, *Microsyst. Nanoeng.* **2023**, *9*, 120.
[22] N. Nitta, T. Sugimura, A. Isozaki, H. Mikami, K. Hiraki, S. Sakuma, T. Iino, F. Arai, T. Endo, Y. Fujiwaki, *Cell* **2018**, *175*, 266.
[23] K. C. Cheung, M. Di Berardino, G. Schade-Kampmann, M. Hebeisen, A. Pierzchalski, J. Bocsi, A. Mittag, A. Tárnok, *Cytometry, Part A* **2010**, *77*, 648.
[24] T. Sun, H. Morgan, *Microfluid. Nanofluid.* **2010**, *8*, 423.
[25] C. Honrado, P. Bisegna, N. S. Swami, F. Caselli, *Lab Chip* **2020**.
[26] C. Petchakup, H. M. Tay, K. H. H. Li, H. W. Hou, *Lab Chip* **2019**, *19*, 1736.
[27] A. Salahi, A. Rane, L. Xiao, C. Honrado, X. Li, L. Jin, N. S. Swami, *Biosens. Bioelectron.* **2022**, *210*, 114346.
[28] D. Spencer, H. Morgan, *ACS Sens.* **2020**, *5*, 423.
[29] A. Salahi, C. Honrado, A. Rane, F. Caselli, N. S. Swami, *Anal. Chem.* **2022**, *94*, 2865.
[30] J. Sui, F. Foflonker, D. Bhattacharya, M. Javanmard, *Sci. Rep.* **2020**, *10*, 1251.
[31] C. Honrado, A. Salahi, S. J. Adair, J. H. Moore, T. W. Bauer, N. S. Swami, *Lab Chip* **2022**, *22*, 3708.
[32] A. De Ninno, R. Reale, A. Giovinazzo, F. R. Bertani, L. Businaro, P. Bisegna, C. Matteucci, F. Caselli, *Biosens. Bioelectron.* **2020**, *150*, 111887.
[33] C. Honrado, N. Michel, J. H. Moore, A. Salahi, V. Porterfield, M. J. McConnell, N. S. Swami, *ACS Sens.* **2020**, *6*, 156.
[34] A. Salahi, C. Honrado, J. Moore, S. Adair, T. W. Bauer, N. S. Swami, *Biosens. Bioelectron.* **2023**, *231*, 115262.
[35] Y. Zhou, D. Yang, Y. Zhou, B. L. Khoo, J. Han, Y. Ai, *Anal. Chem.* **2018**, *90*, 912.
[36] X. Ren, P. Ghassemi, J. S. Strobl, M. Agah, *Biomicrofluidics* **2019**, *13*, 044103.
[37] C. Petchakup, H. Yang, L. Gong, L. He, H. M. Tay, R. Dalan, A. J. Chung, K. H. H. Li, H. W. Hou, *Small* **2022**, *18*, 2104822.
[38] F. Caselli, P. Bisegna, *IEEE Trans. Biomed. Eng.* **2015**, *63*, 415.
[39] C. Honrado, J. S. McGrath, R. Reale, P. Bisegna, N. S. Swami, F. Caselli, *Anal. Bioanal. Chem.* **2020**, *412*, 3835.
[40] F. Caselli, R. Reale, A. De Ninno, D. Spencer, H. Morgan, P. Bisegna, *Lab Chip* **2022**, *22*, 1714.
[41] S. S. Lee, Y. Yim, K. H. Ahn, S. J. Lee, *Biomed. Microdev.* **2009**, *11*, 1021.
[42] M. S. N. Oliveira, M. A. Alves, F. T. Pinho, G. H. McKinley, *Experim. Fluids* **2007**, *43*, 437.
[43] R. Reale, A. De Ninno, T. Nepi, P. Bisegna, F. Caselli, *IEEE Trans. Biomed. Eng.* **2022**, *70*, 565.
[44] F. Caselli, A. De Ninno, R. Reale, L. Businaro, P. Bisegna, *IEEE Trans. Biomed. Eng.* **2020**, *68*, 340.
[45] Y. Feng, J. Zhu, H. Chai, W. He, L. Huang, W. Wang, *Small* **2023**, *19*, 2303416.
[46] Y. Feng, Z. Cheng, H. Chai, W. He, L. Huang, W. Wang, *Lab Chip* **2022**, *22*, 240.
[47] K. E. Richards, A. E. Zeleniak, M. L. Fishel, J. Wu, L. E. Littlepage, R. Hill, *Oncogene* **2017**, *36*, 1770.
[48] Z. Liao, Z. W. Tan, P. Zhu, N. S. Tan, *Cell. Immunol.* **2019**, *343*, 103729.
[49] J. Zhu, S. Pan, H. Chai, P. Zhao, Y. Feng, Z. Cheng, S. Zhang, W. Wang, *Small* **2024**, *20*, 2310700.
[50] A. Rane, J. Jarmoshti, A.-B. Siddique, S. Adair, K. Torres-Castro, C. Honrado, T. W. Bauer, N. S. Swami, *Lab Chip* **2024**, *24*, 561.
[51] K. Torres-Castro, J. Jarmoshti, L. Xiao, A. Rane, A. Salahi, L. Jin, X. Li, F. Caselli, C. Honrado, N. S. Swami, *Adv. Mater. Technol.* **2023**, *8*, 2201463.
[52] M. Liang, Q. Tang, J. Zhong, Y. Ai, *Biosens. Bioelectron.* **2023**, *225*, 115086.

[53] M. A. Raoufi, A. Mashhadian, H. Niazmand, M. Asadnia, A. Razmjou, M. E. Warkiani, *Biomicrofluidics* **2019**, *13*, 034103.

[54] S. Gawad, L. Schild, P. Renaud, *Lab Chip* **2001**, *1*, 76.

[55] J. McGrath, C. Honrado, J. Moore, S. Adair, W. Varhue, A. Salahi, V. Farmehini, B. Goudreau, S. Nagdas, E. Blais, *Anal. Chim. Acta* **2020**, *1101*, 90.

[56] A. Rane, J. Jarmoshti, A.-B. Siddique, S. Adair, K. Torres-Castro, C. Honrado, T. W. Bauer, N. S. Swami, *Lab Chip* **2024**, *24*, 561.

[57] M. Piergiovanni, V. Galli, G. Holzner, S. Stavrakis, A. DeMello, G. Dubini, *Lab Chip* **2020**, *20*, 2539.

[58] J. Cervantes, F. Garcia-Lamont, L. Rodríguez-Mazahua, A. Lopez, *Neurocomputing* **2020**, *408*, 189.